

Article

Patient-Specific Stent Fabrication Using a Seven-Degree-of-Freedom Additive Manufacturing System

John M. Huss ¹, Malachi Lehman ² and Arthur G. Erdman ^{1,*}

¹ Department of Mechanical Engineering, University of Minnesota, 111 Church Street SE, Minneapolis, MN 55455, USA

² Department of Biomedical Engineering, The Pennsylvania State University, 513 Shortlidge Rd, University Park, PA 16802, USA

* Correspondence: agerdman@umn.edu

Abstract: With advances in additive manufacturing technologies, the creation of medical devices which are tailored to the geometry of a patient's unique anatomy is becoming more feasible. The following paper details the capabilities of a seven-degree-of-freedom fused filament deposition modeling system which enables a wide variety of user-control over previously restricted parameters, such as nozzle angle, print bed rotation, and print bed tilt. The unique capabilities of this system will be showcased through the production of a patient-specific tracheal stent using three different methods: segmented overmolding, transverse rastering, and longitudinal rastering. The resulting opportunities and time savings demonstrated by the prints will provide a case for greater implementation of seven-degree-of-freedom manufacturing technologies.

Keywords: seven-degree-of-freedom; additive manufacturing; overmolding; tracheal stent



Citation: Huss, J.M.; Lehman, M.; Erdman, A.G. Patient-Specific Stent Fabrication Using a Seven-Degree-of-Freedom Additive Manufacturing System. *Machines* **2022**, *10*, 1144. <https://doi.org/10.3390/machines10121144>

Academic Editor: Raffaele Di Gregorio

Received: 21 October 2022

Accepted: 28 November 2022

Published: 1 December 2022

Publisher's Note: MDPI stays neutral with regard to jurisdictional claims in published maps and institutional affiliations.



Copyright: © 2022 by the authors. Licensee MDPI, Basel, Switzerland. This article is an open access article distributed under the terms and conditions of the Creative Commons Attribution (CC BY) license (<https://creativecommons.org/licenses/by/4.0/>).

1. Introduction

1.1. Additive Manufacturing for Patient-Specific Medical Devices

Due to advantages such as streamlined preoperative planning, device cost-reduction, and improved clinical outcomes, patient-specific design within the medical devices industry has become increasingly popular [1]. Researchers have found that intraoperative computer technologies for patient-specific device planning are being utilized at a higher rate, while new advantages of patient-specific designs are being demonstrated across a wide variety of medical fields [2]. As planning and design is being improved, there remains a demand for manufacturing techniques which can seamlessly and accurately fabricate patient-specific devices according to medical tolerances. A potential solution exists in additive manufacturing, because it allows for computer-assisted designs to be quickly generated with physical material.

Additive manufacturing techniques such as selective laser sintering (SLS), stereolithography (SLA), and fused deposition modeling (FDM), are currently being used to meet a wide subset of clinical needs. For example, many orthopedics companies are using SLS to create high resolution, small-scale, porous scaffolds, bone plates, and implants [3,4]. Furthermore, SLS can generate fine surface details, overhangs, and ductal structures that might be applied to patient-specific design [5]. The tolerances, specificity, and cost of SLS in many cases make it optimal compared to its manufacturing counterparts [6], and has given rise to greater commercialization of SLS-manufactured medical products in the US [7].

SLA and FDM additive manufacturing techniques provide additional utility due to their cost-effectiveness and rapid realization of geometries. Both SLA and FDM are used in rapid prototyping, construction of anatomical models, and manufacturing of medical devices such as stents, shunting tubes, surgical tools, and other simple static forms [8]. They have become such a universal standard in translating raw ideas into testable prototypes, that some products of SLA and FDM manufacturing have even been developed for clinical use,

including drug-delivery systems, tissue grafts, and tissue scaffolds [9,10]. SLA techniques are usually able to produce higher resolution models compared to FDM, while FDM systems are usually cheaper, easier-to-use, and can access a wider array of rigid and flexible deposition materials [11]. Both tools have been highly beneficial to the patient-specific device design space, particularly due to their cost-effectiveness in producing anatomical molds. Finally, creative modifications to the above techniques have been employed to solve complications associated with radial or highly non-uniform geometries. A six degree-of-freedom FDM printing system has been created wherein a filament deposition nozzle mounted on a serial motor arm allows the user to access more surfaces of a workpiece [12]. Similarly radial FDM systems which are capable of depositing along curved or cylindrical print surfaces have also been formulated [13]. Finally, a seven-axis serial robotic additive manufacturing system has been suggested by the large additive manufacturing technologies company, Stratasys [14]. These technologies represent what may be the future standard in patient-specific device manufacturing, providing more tools to address the unique geometric challenges of human anatomy.

1.2. Limitations of Current Additive Manufacturing Methods

While the current scope of technologies fulfills many specific commercial and clinical needs, several limitations prevent any singular method from expanding beyond its set of established use-cases. SLS manufacturing is limited in large part due to the post-processing of the workpiece, wherein excess powder must be removed from porous or ductal spaces [15], limiting the creation of certain geometries. In addition, some toolpaths of an SLS print are restricted or entirely unfeasible due to the thermal deformation of the part during sintering [16,17]. Even allowable paths may sometimes require scaffold networks to be constructed if there is large separation between two branches of the workpiece in 3D-space. Finally, the segmented nature of the sintering process, wherein material is fused in a series of layers, can produce variations in molecular grain structure which introduce undesirable macro-scale anisotropy to printed structures [18].

SLA printers are similarly limited in the geometries they can create. Because parts are being constructed from a photocured resin bath, there is no solid or dense surrounding material to support larger structures as they are being printed [19]. Therefore, as with SLS, scaffolds must frequently be built to prevent larger prints from shifting or collapsing. The post-processing removal of these scaffolds often blemishes the surface of the part, or entirely limits some hollow structures from being created. SLA also only gives partial user-influence over the global structural properties of a part, limited to part orientation on a print-bed, layer-height, and curing methods [20].

FDM is perhaps the most limited with regard to patient-specific design, with primary drawbacks stemming from the method by which FDM adds material to a workpiece. Strands of filament are heated, extruded, and deposited along a toolpath to build a geometry, giving rise to characteristic layer artifacts created by the orientation of the layered material [21]. These artifacts pose potential problems for devices that must be manufactured with tight surface-finish tolerances and are difficult to mitigate without post-processing [22]. In addition, typical FDM methods cannot realize complex features or enclosed hollow structures without making significant sacrifices to accuracy, surface finish, or strength [23,24]. Similar to SLS and SLA methods, these types of FDM prints require scaffolds to support toolpath layers suspended in 3D space, meaning hollow, branching, or overhanging structures are very difficult to produce.

Fundamentally, these limitations can be tied to a universal constraint among systems. Current methods rely on fixed cartesian or radial coordinate systems to drive the deposition or sintering toolpath, thus limiting user-control over directional mechanical properties and demanding some form of post-processing which reduces the accuracy of the final structure. Without universal influence over the toolpath, the scope in which each method can be applied must be narrowed to a particular subset of geometries and structures. Such limitations inhibit patient-specific design, as they cannot account for the dynamic demands

that each unique person's anatomy might present. This paper will explore the advantages of a new seven-axis fused filament deposition 3D printer. This system will allow for enhanced user-control over the deposition toolpath and layer orientation of prints. These unique advantages will be showcased through a method and workflow for creating a tracheal stent from patient-specific scan data.

1.3. The Seven-Degree-Of-Freedom Additive Manufacturing System

The FDM system constructed for this research is able to reposition parts as they are built in order to manipulate the orientation of deposited material and give access to exposed surfaces of the workpiece. Specifically, the base of such a system, acting as a traditional build plate, can tilt and rotate independently of the filament nozzle, which itself can tilt laterally and transversely, as well as move by way of a gantry in the three traditional X, Y, Z directions. This system, shown in Figure 1 [25] and demonstrated in Videos S1–S4, has been designed and built at the University of Minnesota for a mechanical engineering PhD thesis project by Dr. John Huss. The inverse kinematics and other details of the robotic system can be found in [26].

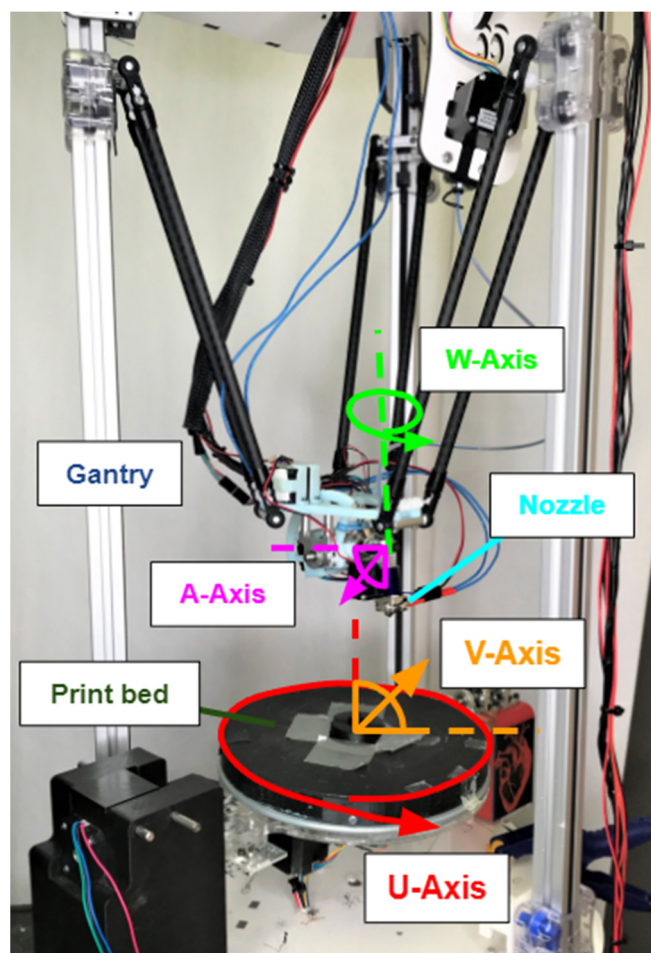


Figure 1. Seven-degree-of-freedom 3D-printing system designed by Dr. John Huss. The build plate rotates along the U-axis and tilts along the V-axis. The filament nozzle moves in the X, Y, and Z directions by way of the gantry, tilts laterally along the W-axis, and transversely along the A-axis.

When additively manufacturing devices for medical applications, one can imagine scenarios where devices must contain widely spaced, ductal, weblike, or highly non-uniform geometries with predictable structural properties. Oropharyngeal airways, heart valves, and medical stents are examples where the devices must take on highly non-uniform geometries with tightly regulated material and structural properties [27], limiting current

additive manufacturing methods from impacting their production in a significant way. These applications are particularly well suited to the seven-axis system because of its ability to fabricate complicated and non-uniform shapes. Parts require little, if any, sacrificial support structure because newly deposited material can be supported by the model itself. This greatly reduces the amount of support material used and discarded as waste and provides more flexibility while printing part features, giving the user increased control over local deposition density or other properties. This self-supporting capability is combined with a five-degree-of-freedom print head to allow for changing layer line directions as well. Finally, the general nature of this printer allows it to print on surfaces that are more complex than two-dimensional build trays and part layers [28]. This leads to the possibility of printing onto existing additively manufactured parts, or more interestingly, objects that are not additively manufactured, such as machined parts, or anatomical structures.

To fully demonstrate and evaluate the benefits of the seven-axis system, a series of methods was devised to manufacture both a patient-specific anatomy model of a tracheal airway, and an airway-supporting stent prototype to adhere to its outer surface. A future tracheal stent device based on the concept introduced here, could potentially be used in patients with a stenotic, or narrowed, tracheal airway [29]. The stent example demonstrates the system's ability to both control material deposition properties and produce geometries with open spaces. The airway anatomy mold will demonstrate the system's ability to follow curvilinear toolpaths along cylindrical surfaces according to patient-specific medical data. Finally, these combined models will demonstrate the system's ability to enable device processing parallelization and streamlining.

The methods were chosen to highlight the unique capabilities afforded by the seven-axis system, rather than the clinical efficacy of the product. The produced stent is meant to be a prototyping example rather than a clinically viable medical device. Therefore, considerations that would be important in a clinical use, such as the biocompatibility of the filament used, the deployment of the stent itself, and mechanical integrity of the stent during medical use, were not showcased. Further directions for the system's evaluation and use will be addressed below.

2. Materials and Methods

2.1. Overview

The methodology introduced in this paper follows a sequence summarized in Figure 2. First a series of mathematical and programming steps was taken to transform a conventional standard triangle language (STL) printing file of a patient trachea airway scan to a stent tool path compatible with the seven-axis printing system. The trachea airway was printed in three different ways: segmented, transversely rastered, and longitudinally rastered, to highlight the system's key advantages. Finally, a patient specific stent was printed onto the surfaces of the various trachea models.

In summary, these steps create a replicable process which allows for an STL file of a patient airway to be transformed into a physically printed stent device formed directly to its anatomy. The individual steps are covered in more detail below.

2.2. Trachea Model Generation

The first step is to transform a magnetic resonance imaging (MRI) scan from a patient into an STL file which captures the geometry of a specific organ. Typically, to obtain a 3-dimensional STL mesh file of a patient's anatomy, a process called segmentation is done. In segmentation, a computed tomography scan or a stack of MRI images are opened in a software which allows the user to manually or automatically identify and separate areas of tissue in each image [30]. For the purposes of this paper, a patient-specific STL model of a trachea was downloaded from an online repository of anatomical 3D files and segmented via the Mimics version 19.0 [31] software package. The tissue model of the trachea was then inverted using a Boolean operation to recreate a model of the tracheal lumen rather than the tracheal tissue itself. A locking base was added to the bottom of the section of trachea to

allow for mating with a matching receptacle located in the center of the seven-axis printer build plate, shown below in Figure 3a,b, respectively. The locking receptacle in Figure 3a was printed directly onto the center of the build plate to ensure it was located in a known position. Locking the trachea model into the printer using this mechanism ensures it does not move while material is added and allows for additional trachea molds to be swapped between prints.

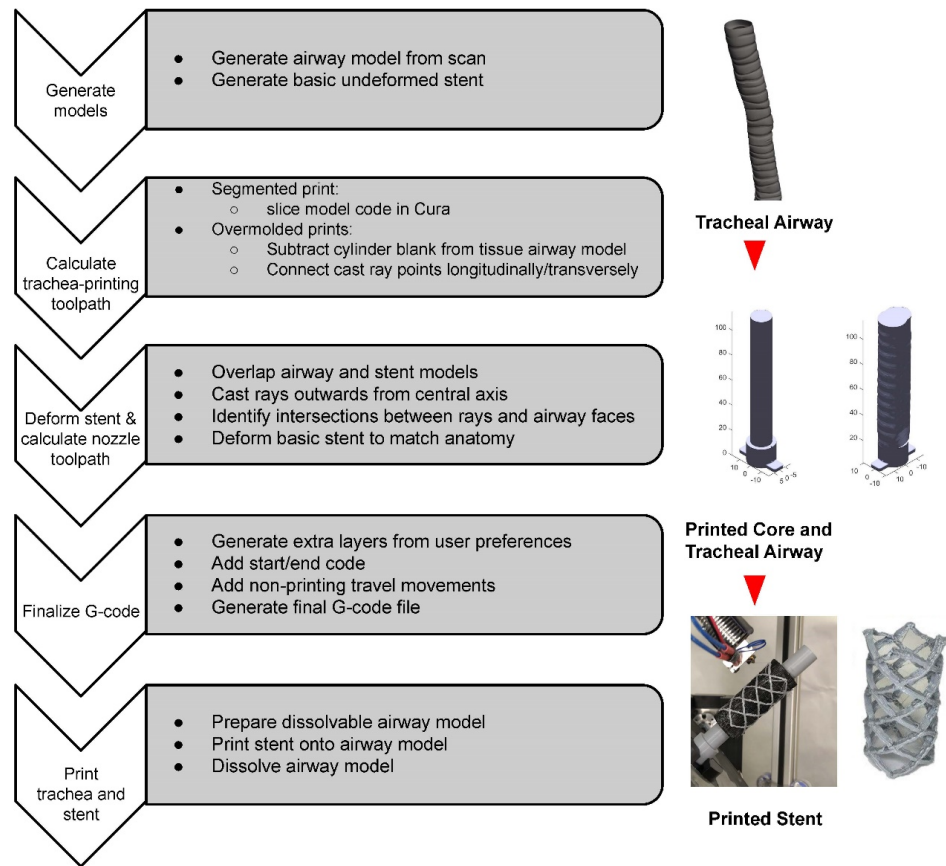


Figure 2. Flowchart describing the patient stent manufacturing process.

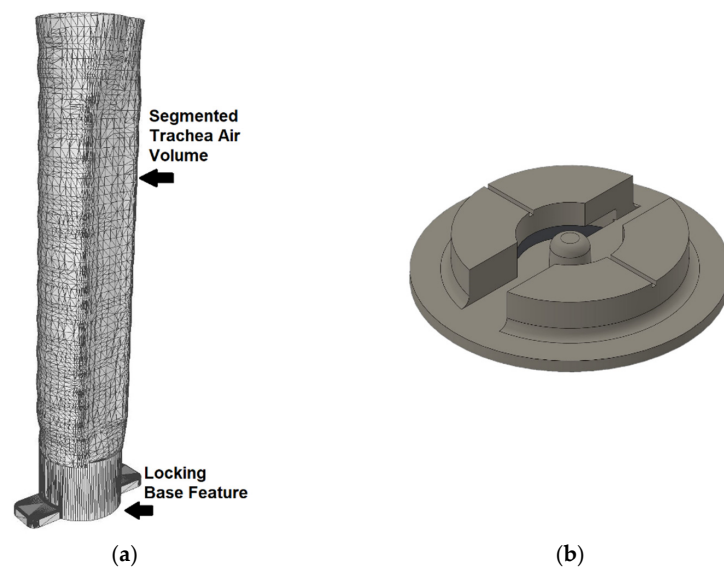


Figure 3. (a) The trachea mesh with added base for registration and locking. (b) The matching 3D-printed locking receptacle.

2.3. Toolpath Generation for the Trachea Airway Print

Three different methods were utilized to convert the STL file into a printed tracheal airway model: traditional FDM, transverse overmolding, and longitudinal overmolding. Beginning with the traditional FDM method, the STL file was imported to the Ultimaker Cura v3.3.0 [32] slicing software which turns the geometry into a conventional three-axis G-code. The G-code was then loaded into a Creality3D CR-10 traditional three-axis printer [33] which executed a segmented, layer-by-layer print of the tracheal airway. This segmented print acts as a baseline, while the transverse and longitudinal overmolding methods demonstrate the seven-axis system's unique capabilities.

The transverse and longitudinal overmolding methods highlight potential process parallelization using the seven-axis system. Given that much of the tracheal airway is made up of filler material, an "anatomy blank" can be created that approximates invariant features such as the inner core of the model. This blank is subtracted from the patient specific details, like the variable trachea tissue surface, which can be added back on later using the seven-axis system, saving time and resources. For a trachea, this blank can be a cylinder with a diameter slightly smaller than the expected minimum diameter of the airway, shown in Figure 4.

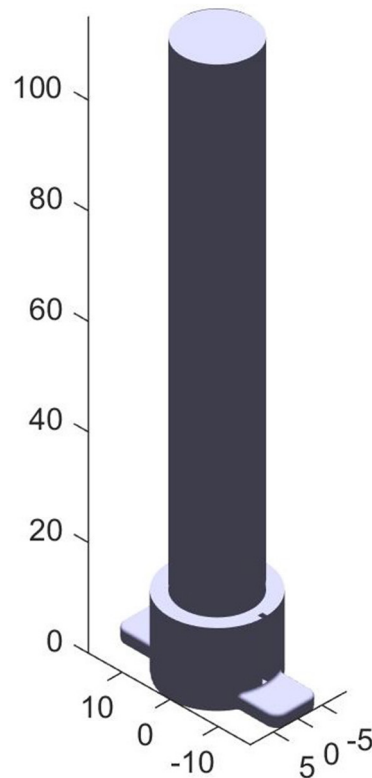


Figure 4. This blank represents the bulk air volume within a patient's trachea. The patient specific model will be added on the surface of the blank. Units in mm.

From this point, the seven-axis system can print on the surface of the blank using the transverse and longitudinal rastering methods. The transverse method adds material by rotating the model underneath the nozzle while slowly maneuvering from the bottom to the top of the model. The longitudinal method deposits material by following along the long axis of the blank, rotating a user-specified amount of 2.5 degrees, and then moving back in the other direction while depositing additional rows. Each of these methods requires modification of the STL file to obtain a toolpath which can be interpreted by the seven-axis system.

This toolpath was created through the following process. First, candidate toolpath points were generated such that they formed an even distribution of points within a hollow

cylindrical volume, with an inner radius equal to the radius of the blank and an outer radius slightly larger than the maximum radius of the patient’s airway. The points were chosen based on the parameters in Table 1 and are shown (with many points removed for clarity) in Figure 5.

Table 1. Slicing parameters used in the final toolpathing.

Parameter	Value	Description
Ri	7.25 mm	Radius of the blank
Length	70 mm	Length of section to print
Longitudinal spacing	0.5 mm	Vertical spacing of points
Angular Spacing	2.5°	Angular spacing of points
Layers	30	Max number of layers to generate
Offset	35 mm	Distance from base to start
Retraction	1 mm	Nozzle retraction during movement

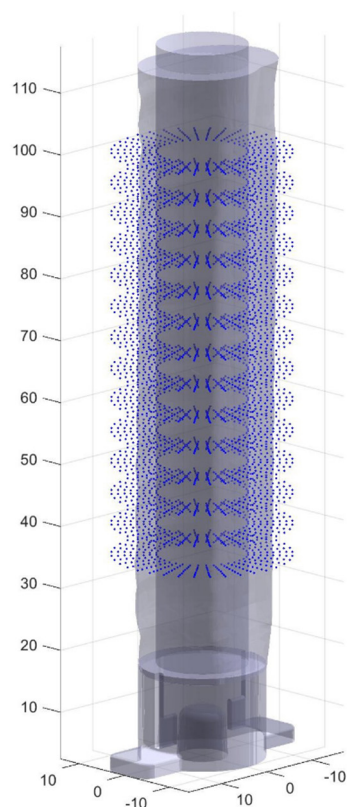


Figure 5. Points are generated as candidates for the final toolpath.

Rays were then cast from the central axis of the blank through the candidate points surrounding the blank. Using a ray/triangle intersection algorithm each point was determined to be inside the final patient specific model and therefore kept as a final toolpath point, or outside the model and rejected. A given point was considered inside the model if its distance from the central Z axis (the norm of its (X,Y) coordinate) was less than the norm of the triangle/ray intersection point of the ray passing through the point. The final selection of points were then connected together to create a toolpath, which is where the two methods diverge. Longitudinal toolpathing connects the points along the long axis of the airway first in a series of vertical lines, and transverse toolpathing connects them around the blank into a series of rings. While ultimately both toolpaths cover the same volume, different axes are primarily utilized. Primarily (X,Y,Z) linear motion is used in the transverse toolpath, while more rotation around the center of the part, defined from here as the U axis of rotation (see Figure 1), is used in the transverse toolpath. The final step was to

connect the often disconnected printing segments (since many candidate points outside of the final model were removed) with nonprinting retracted moves above the surface of the object. The resulting toolpaths are shown below in Figure 6, again with many points removed for clarity.

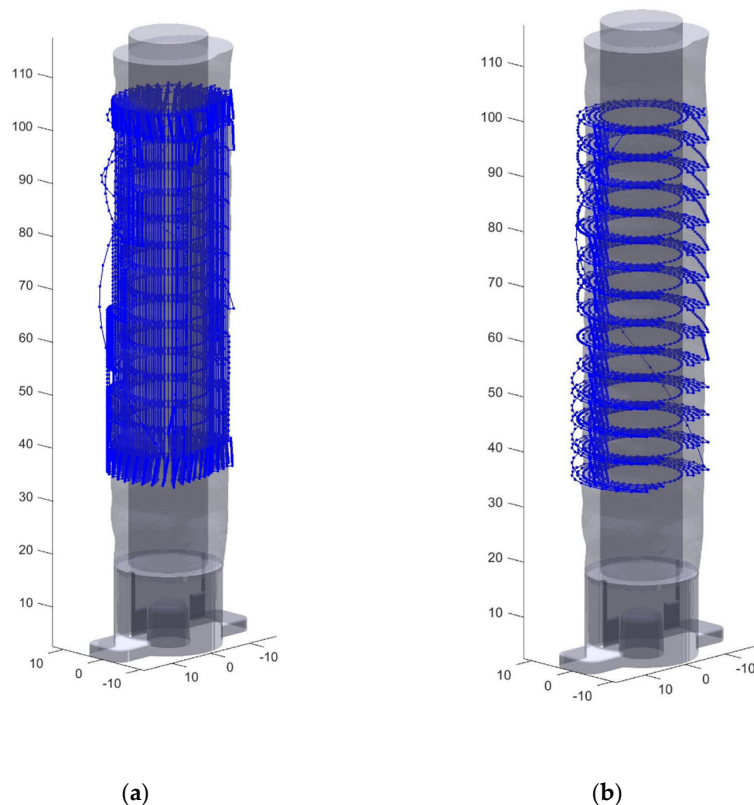


Figure 6. Toolpaths generated for stent print (a) Simplified view of the longitudinal toolpath generation (b) Simplified view of the transverse toolpath generation.

Both of these developmental processes, longitudinal and transverse rastering, result in completely solid layers rather than the traditional shell and infill style typical of FDM, and an unfortunate loss of much of the fine surface detail. Once a toolpath was created, a blank can be loaded into the printer and a file can be run to create the final trachea model out of a dissolvable PVA material. The meshes were compared to see exactly how their accuracy compared to standard FDM printing.

2.4. Stent Model Generation and Transform

The next step is to generate the toolpath for the patient specific stent based on the trachea model. This process was initiated using a basic stent model consisting of a series of eight lines forming a helix pattern. The helix was given a 40 mm Z axis offset from the printer bed to allow the printer nozzle to have adequate access to the side of the trachea model without colliding with the locking base features. A script was created in MATLAB R2018b (MATLAB 9.5) [34] to both generate this basic stent design and import the STL file faces and vertices. The sample stent design is shown below in Figure 7a. After aligning the coordinate systems of the trachea model and the proposed stent design, seen below in Figure 7b, this script determines how to deform the basic stent to match the patient model.

The script accomplishes this by casting hundreds of rays from the central axis outwards through each of the stent struts and through the surface of the trachea model. The hundreds of rays are shown extending through the airway STL in Figure 8a. The rays were programmed to be spaced 0.05 mm apart, so they appear as a helical plane. The trachea STL model created had 25,530 faces and 11,269 vertices. The intersection points of the cast rays and the trachea mesh faces were finally determined using a ray/triangle

intersection algorithm first developed by Moller and Trumbore [35]. The algorithm completes a search by examining all rays in order and checking each ray against all triangles. Shown in Figure 8a, this model contains 25,530 faces, which were cast through by 8000 rays, resulting in 204,240,000 calculations if each ray intersects the last triangular face checked. In practice, this number is substantially lower because once a ray is found to intersect a face, the algorithm moves onto the next ray. Once the intersection points of each ray were determined, the stent radius was deformed to match each of the intersecting points on the airway model, plus a small 0.1 mm offset so that the stent is on top of the surface, shown below in Figure 8b. Extra layers were then added by repeating the patient specific stent toolpath at the specified layer height to give the stent the desired thickness. Using at least three layers at 0.15 mm thickness provided a stent that was strong enough to survive the post processing. Ten layers were used for most testing and images shown.

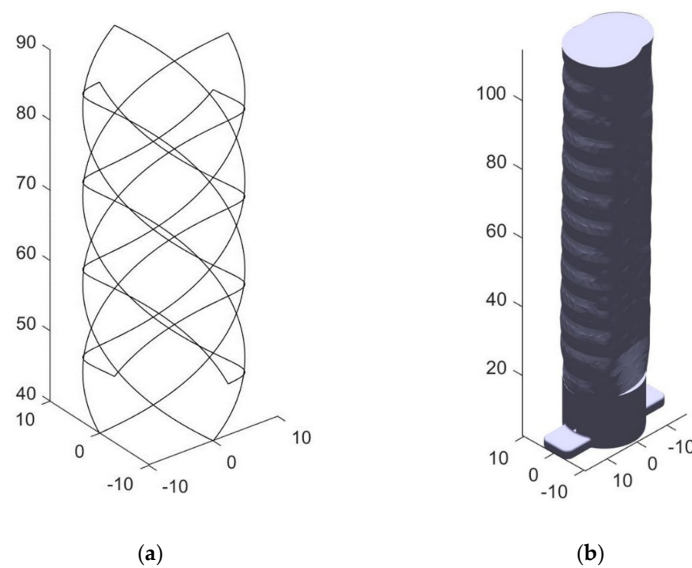


Figure 7. (a) The untransformed stent model composed of eight helical struts, four in each direction (b) The stent is overlaid onto this trachea model.

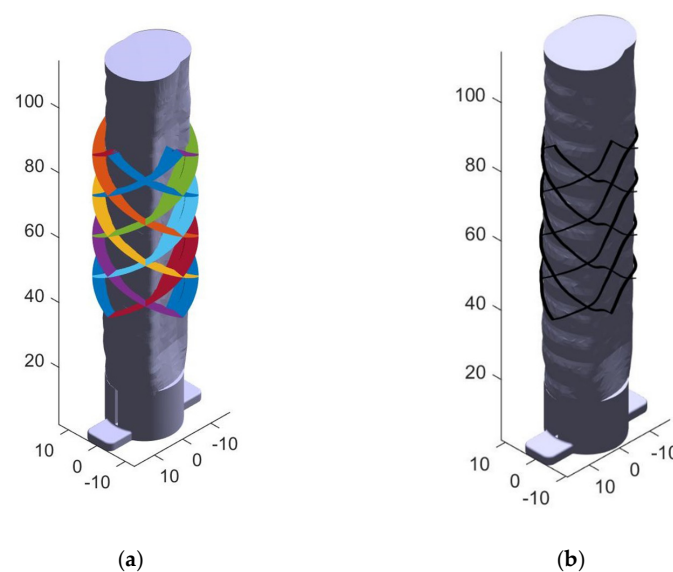


Figure 8. (a) Many rays are cast outwards through the trachea walls from the central axis. Each color represents a different pass of the print head in the final toolpath. (b) The intersection points are used to deform the basic stent struts and extra layers are added as specified by the user.

2.5. Nozzle Angle Calculation

With a tool path generated, the printer nozzle position and angle could be calculated. Referring to Figure 9, the nozzle must tilt 90 degrees sideways relative to the build plate and to access and print on the airway model from the side. The bed also must be tilted on the V axis, that is, the axis which is manipulated according to the reference X axis of the ground frame (see Figure 9), at 45 degrees so that the airway model will be below the extruded plastic. The trachea model will then rotate on the U axis through the center of the build plate and the nozzle will move axially along its length. For the best print quality it is imperative to keep the nozzle as perpendicular to the surface as possible, matching the contours of the airway.

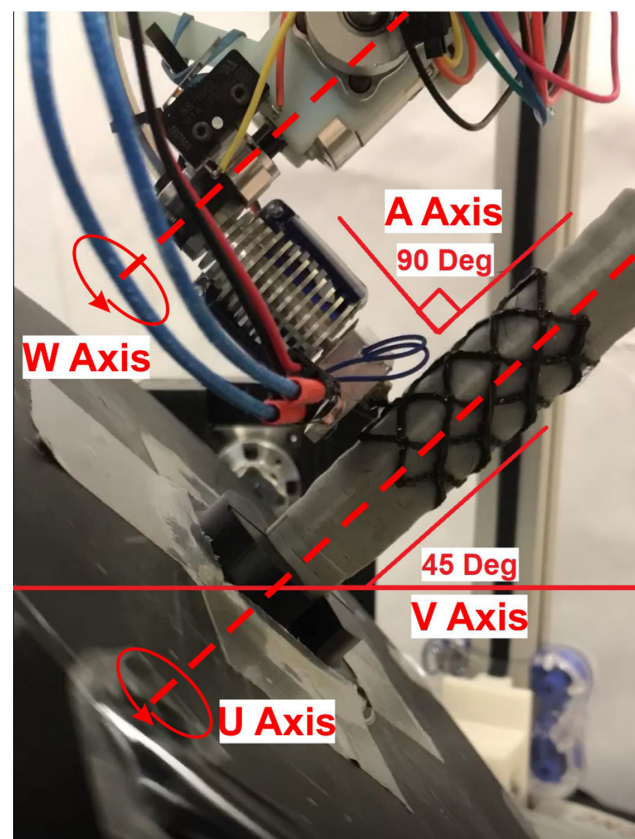


Figure 9. The stent is printed onto the patient's trachea model from the side. The object frame rotates with the U axis, while the V frame is static and tilted 45 degrees.

To communicate the original toolpath to the seven-axis system, a transform was performed using two separate reference frames: the rotating object frame (centered at the U-axis) and the stationary V frame. X , Y , and Z were selected to represent coordinates within the object frame, which rotates and tilts on the print bed with respect to the ground frame, and X_v , Y_v , Z_v were selected to represent coordinates in the stationary V-frame, which only tilts with the V axis of the tilting bed. U was chosen to represent the current angle of the continuous rotation axis through the center of the bed, and V_z is the constant 5 mm vertical offset between the reference frames due to the construction of the printer. Shown in Equation (1), this transform results in a series of coordinates which map the movement of the nozzle system.

$$\begin{bmatrix} X \\ Y \\ Z \\ 1 \end{bmatrix} = \begin{bmatrix} \cos(U) & -\sin(U) & 0 & 0 \\ \sin(U) & \cos(U) & 0 & 0 \\ 0 & 0 & 1 & V_z \\ 1 & 0 & 0 & 0 \end{bmatrix} \times \begin{bmatrix} X_v \\ Y_v \\ Z_v \\ 1 \end{bmatrix} \quad (1)$$

As stated, it is also imperative that the nozzle remain normal to the surface of the airway model to preserve print quality and properly extrude material. To accomplish this, the nozzle compensation angle, W , must be calculated for each point on the stent. Figure 10 below shows how the coordinate system rotates around the U -axis as the printing process progresses and what the W angle represents. The U -axis is a rotational axis that is congruent with the linear Z axis of the object frame. The W axis is measured in reference to the V frame and does not rotate with the object.

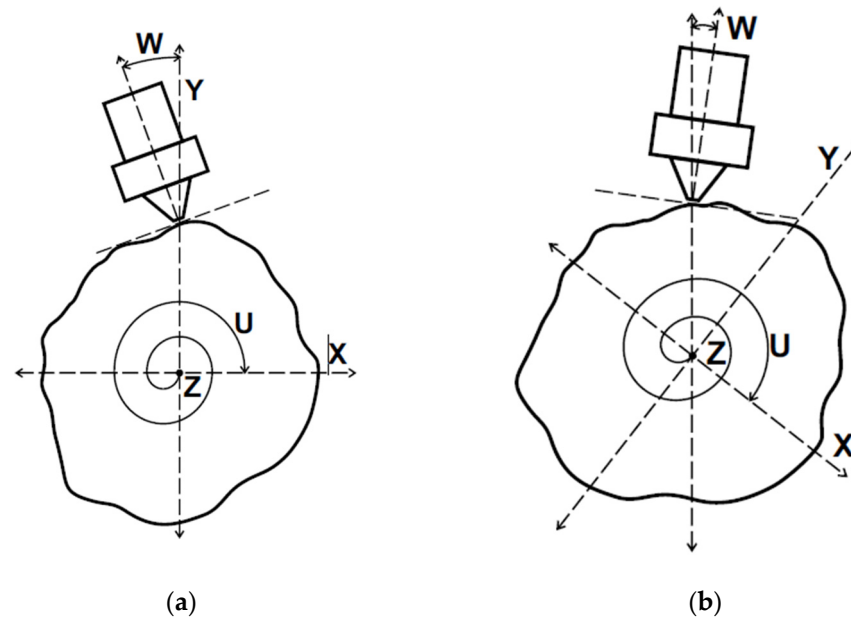


Figure 10. (a) The trachea model viewed end-on during stent printing. (b) The object frame and model rotate while the nozzle follows the surface contours.

The W angle of any given point is a measure of the slope in degrees at that particular point on the airway model. Since this model is made of discrete points, the W angle at any point n was determined by the arctangent of the line between the current point n and the previous point $n - 1$ relative to a flat reference line. The slope equation must also take into account the round surface, and handle angular positions starting under 360 degrees and wrapping around 0 by using the modulo operator. Equation (2) calculates W according to these relations.

$$W_n = \text{rad2deg}(\text{mod}(a \tan 2(Y_n - Y_{n-1}, X_n - X_{n-1}) - a \tan 2(Y_n, X_n), \pi) - \pi/2) \quad (2)$$

The resulting W_n angle produced by the function was then filtered to produce smooth continuous motion of the W axis using a ten-point moving average filter. However, since a filter introduces undesired phase delay into the new W angle data, the data was passed back through the filter in reverse to remove the phase delay using zero-phase digital filtering. Performing this filter operation twice, once forward and once reversed, doubles the effective order of the chosen filter transfer function and squares the magnitude of the input transfer function. The ten-point moving average transfer function was chosen with these effects in mind. The results of the filtering process are shown below in Figure 11. Each line in the plot represents one of the eight supporting struts of the stent. In the figure below the left end of the x -axis is the portion of the stent closest to the printer bed beginning at 40 mm from the surface, and the right side is the highest portion of the stent ending at 90 mm from the bed surface.

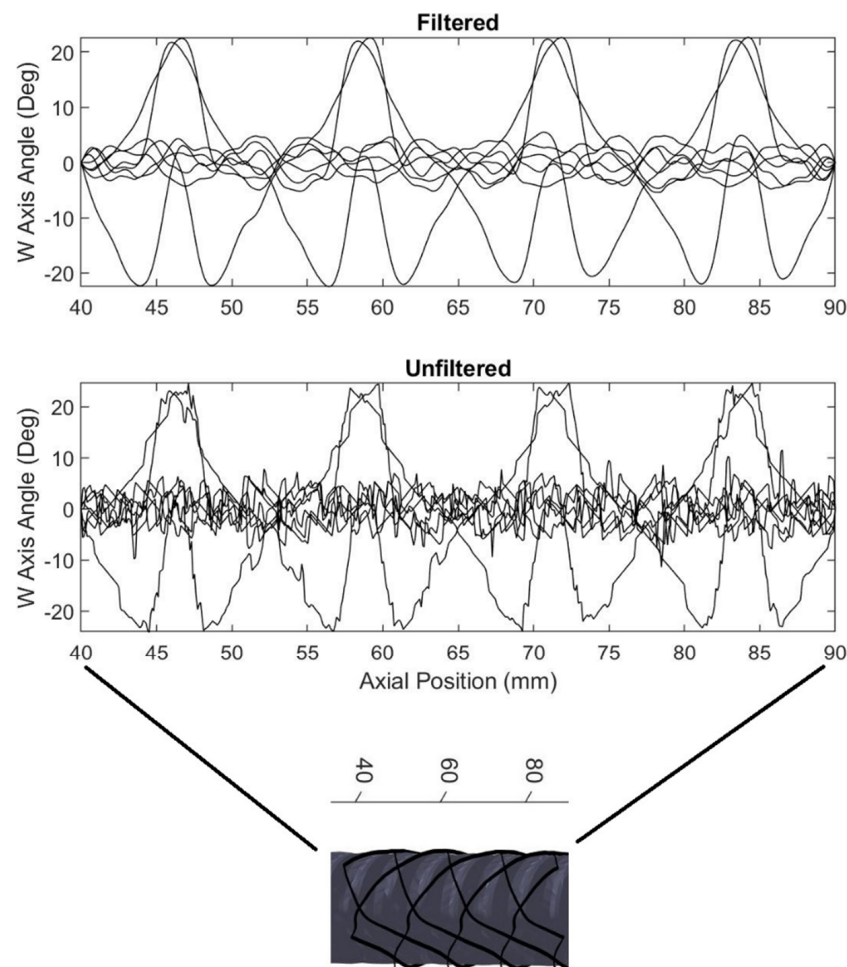


Figure 11. A moving average filter is used to smooth the W axis motion as the stent prints. Each line in the plot represents one of the eight stent struts.

2.6. G-Code Finalization

With the printing movements computed, the final toolpath can be calculated. A set of various commands were created to form the start and end G-code including heating, feeds and speeds settings, homing, and a pause feature that allows time to connect the airway model upon which the stent is printed to the locking receptacle after homing is complete. Non-printing travel commands were added next, between each printing move. These commands retract the nozzle and filament away from the surface, interpolate extra coordinates between the end of one printing segment and the start of another, and then un-retract the nozzle back into place on the model surface at the start of the next printing move. Once all printing moves have been completed, a standard end code is executed, turning off the heaters and fans, and pausing for the completed stent to be removed from the system. The toolpath is shown in several forms in Figure 12.

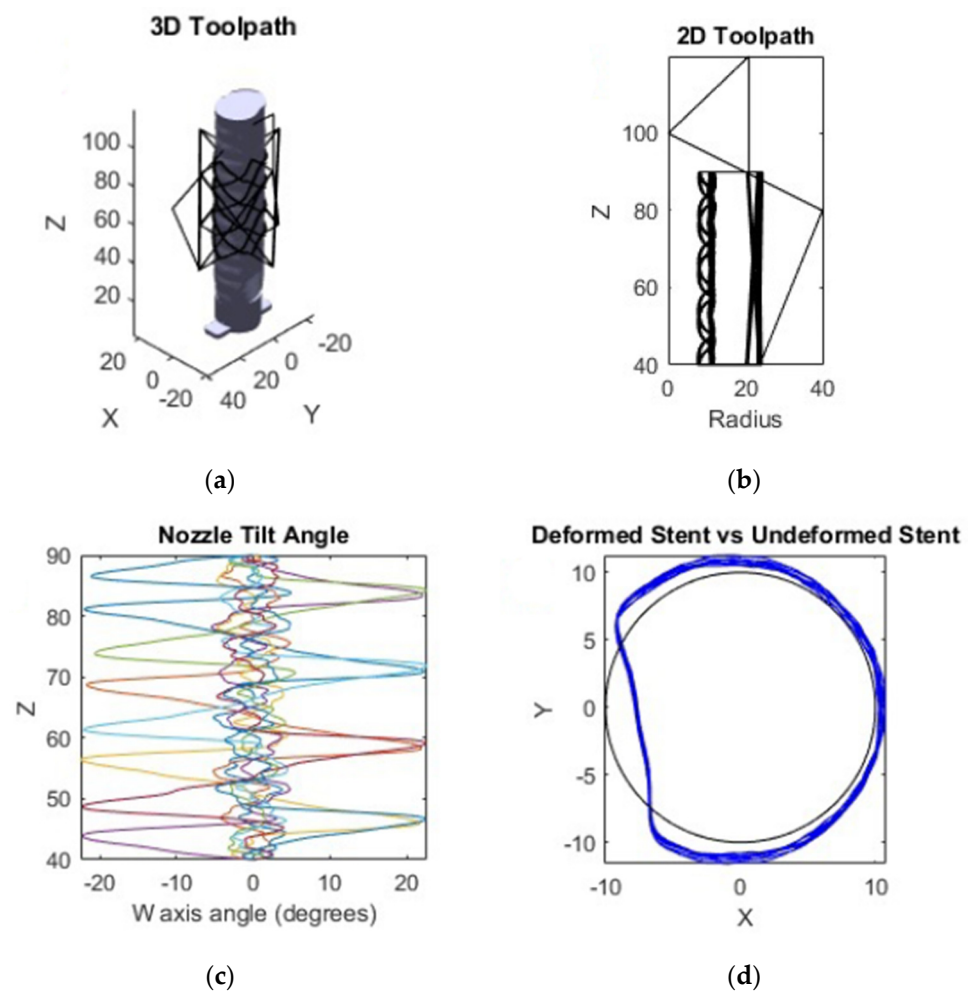


Figure 12. (a) The final toolpath in the object frame. (b) The toolpath in the non-rotating V frame. (c) The W axis compensation angle as the stent prints, with each color denoting a single radial pass of the extruder. (d) The transformed stent vs. undeformed base stent as seen from above.

2.7. Printing of the Stent

The stent printing G-code file was executed in the same way any other G-code file would, except that it additionally manufactured an object onto an existing geometrically complex object by following the toolpath generated earlier. In this case, the existing object was a dissolvable PVA printed airway model that can be dissolved after the stent is created. The trachea model rotates underneath the printer nozzle, which is oriented perpendicular to the surface of the airway as seen in Figure 9. Due to the complexity of a seven axis system, there are limitations to the range of positions that are calibrated. Staying closer to the neutral position results in a more accurate print because the printer is calibrated in the neutral position. As much trachea material as possible is removed by hand before letting the remaining PVA material dissolve away completely in warm water. The whole process of removing the inner core takes as little as five minutes with a bit of manual labor as the PVA softens.

3. Results

With regard to testing the physical products of the process, both the final medical device and the overmolded trachea were evaluated. The stent print details were observed to verify radial orientation of the print layers, while the quality and utility of the trachea airway print surfaces were analyzed through a Hausdorff and time-to-print analysis. A Hausdorff analysis measures the distance from every point of a reference mesh to the closest point on a target mesh [36].

3.1. Stent Print

The final stent is shown below in Figure 13 printed on a standard and overmolded airway model. A stent with the airway model dissolved is also shown. Finally, Figure 14 shows a close up of the layers of the stent oriented along a specific axis.

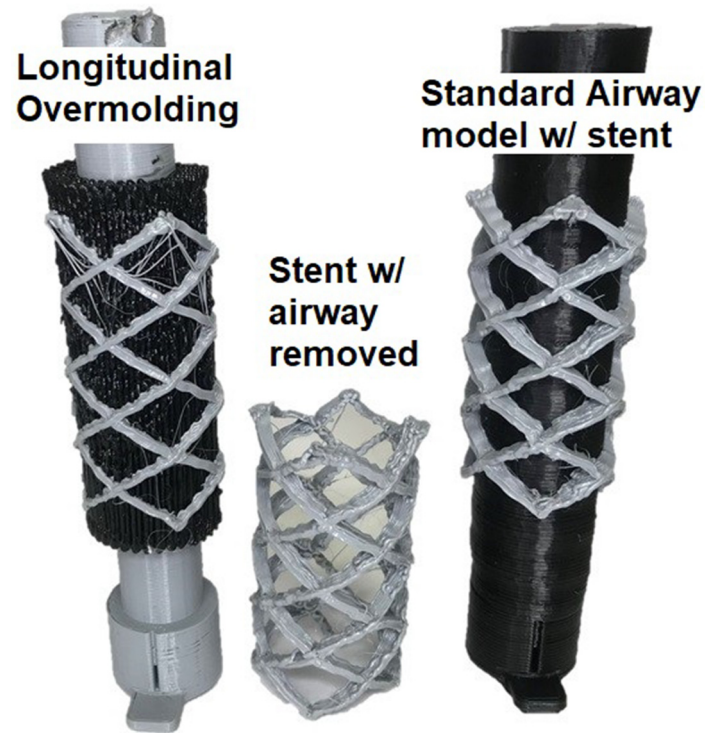


Figure 13. The stent is once again printed onto the patient's trachea model.

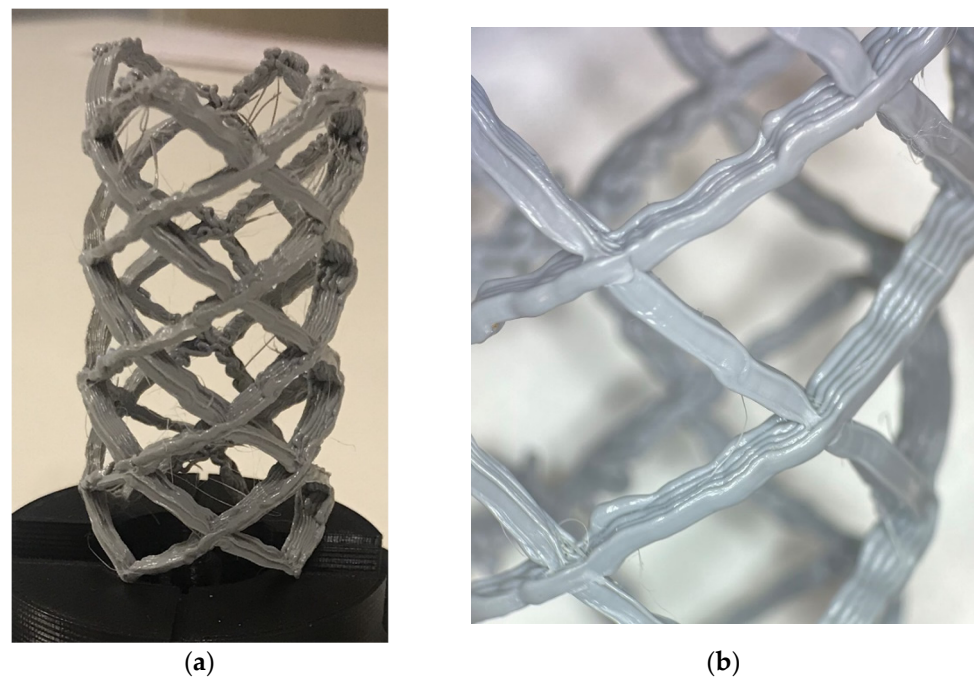


Figure 14. (a) The completed stent model. (b) Close up of the radial layers of the stent.

3.2. Trachea Airway Prints: Mesh Analysis

A 3D scan of the surfaces of the final airway prints is shown in Figure 15. On the overmolded prints, many of the surface features are left appearing rough, such as the repeating pattern of bulges due to the trachea cartilage. A Hausdorff analysis was performed to determine the overall accuracy and repeatability of the printed trachea models in the segmented and overmolding methods. Three of each standard, longitudinal, and transverse trachea models were examined here. All nine models were truncated to be the same height of 70 mm, for a proper comparison.

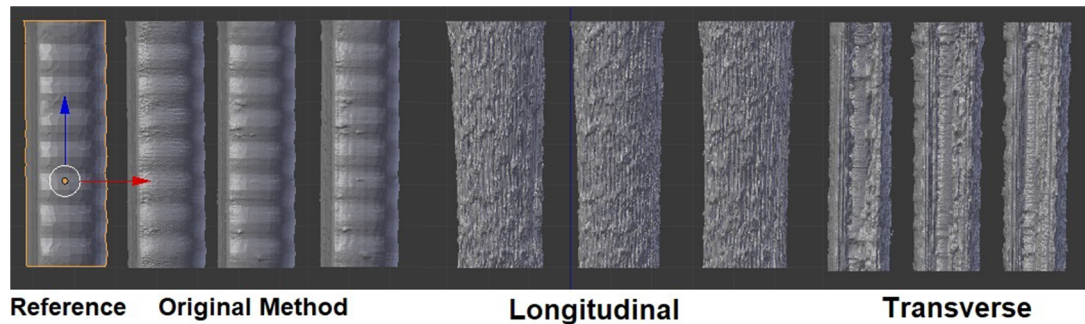


Figure 15. Comparison of the original, longitudinally rastered, and transversely rastered airway models.

In this case, all nine of the scanned meshes in Figure 15 were compared to the reference mesh sliced directly from the original Mimics file. A heatmap showing root mean square (RMS) values for each point from the analysis is also shown below in Figure 16. The higher the value, the less accurate the mesh. Unfortunately, Meshlab 2016 [37], the software package used to generate the heatmaps in Figure 16, does not provide an absolute scale for these analyses. Each model uses a relative scale, where red indicates the lowest value and blue indicates the highest for that specific model.

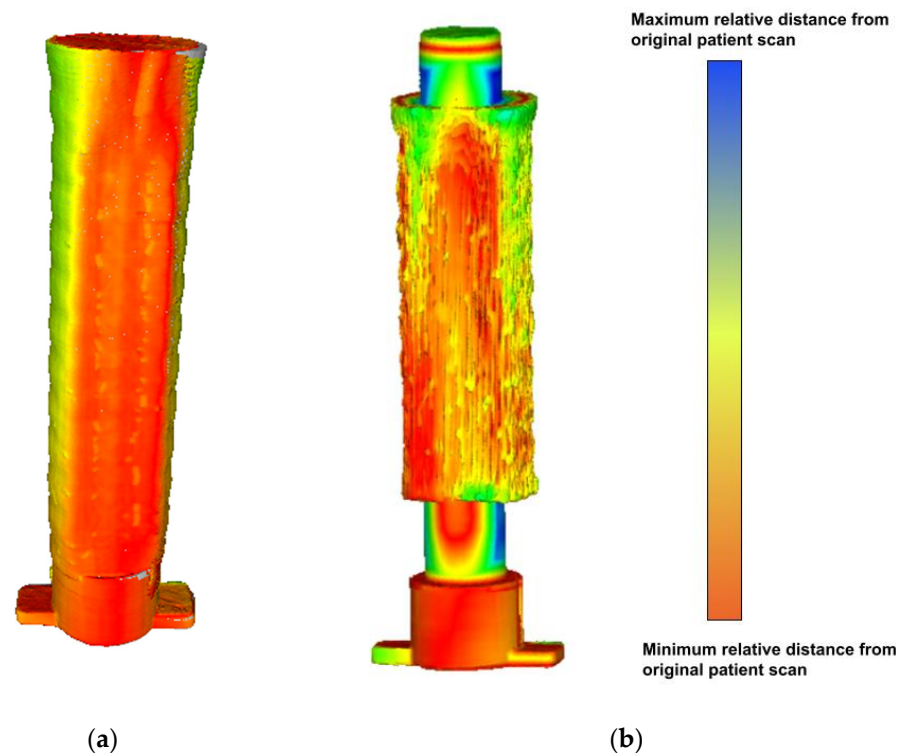


Figure 16. (a) Sample Hausdorff heatmap for the standard airway model. (b) Sample Hausdorff heatmap for the longitudinal airway model.

The RMS Hausdorff values are recorded below in Table 2, along with the averages and standard deviations of the three samples in each group.

Table 2. RMS Hausdorff distances for each printing method.

Airway Hausdorff RMS (mm)	Sample 1	Sample 2	Sample 3	Mean	SD
Standard	0.2997	0.4275	0.3713	0.3662	0.052
Longitudinal	0.8602	0.7921	0.7769	0.8098	0.036
Transverse	0.8272	1.3325	0.8673	1.0090	0.229

3.3. Comparisons for Airway and Stent Printing

The three methods chosen to print the trachea airway and the stent were compared based on the time they contributed to the entire stent fabrication process. Table 3 shows that once segmentation is complete, the printing time of the stent is relatively short.

Table 3. Time savings between standard and alternative methods in hours.

Time (Hours)	Segmenting	Blank	Airway	Stent	Total (Blank Not Included)
Standard	2.00	-	1.25	0.25	3.50
Longitudinal	2.00	0.50	0.50	0.25	2.75
Transverse	2.00	0.50	1.50	0.25	3.75

4. Discussion

4.1. Implications of the Patient-Specific Stent Case Study

The stent print represents an example of a patient-specific medical device prototype which highlights the unique advantages of the seven-axis printer system. The stent's geometry contains properties which could not be reconstructed without the system's ability to manipulate the influence of gravity and print on a rotating surface. For example, in Figure 14, it can be observed that because scaffolding was not required, the surface of the part remains unblemished. In addition, curvilinear print layers form the entirety of the stent body. Compared to other additive manufacturing methods, a primary observation about this system's utility can be made. While many available additive manufacturing technologies are capable of producing various types of medical stents [38,39], the system introduces novel material deposition directional control which can positively impact the strength and stiffness properties of the finished part [26]. For example, giving the user control over the layer orientation, allows for creation of structures with applications in high-stress biological environments. Overall, the particular created device could not be used in clinical practice at this level of development, but indicates that it is highly reasonable that patient-specific devices like a large-scale airway stent could be generated quickly and effectively using the methods outlined.

4.2. Evaluation of Processes Parallelization

Although requiring print quality to be sacrificed in the process, the trachea airway prints represent additional manufacturing capabilities made available by the seven-axis system. The system allows the user to parallelize the printing of a large volume of the anatomy mold with the segmenting of the patient's unique anatomical surface features. A manufacturing pipeline could theoretically be developed wherein patient data is received, segmented, and immediately transferred to a pre-printed anatomy blank, saving time in the translation of medical data into a patient specific device. The parallelization methods will require significant development however, with only the longitudinal overmolding generating moderate time-savings. The overmolded models also have fewer or no remaining trachea cartilage rings or defining features of the original patient anatomy. In addition, they have significantly higher Hausdorff error values than the segmented

models. One may therefore assume these models are poor representations of the original anatomy. Comparing the overmolding methods to each other, the longitudinal models are more accurate than the transverse models despite the fact that the transverse models do clearly at least capture the rings of cartilage. This can be explained by examining the mechanics of the system; the rotation axis through the centerline of the trachea model, U, is less accurate than the (X,Y,Z) axes used in the longitudinal method due to the fact that the nozzle position in Cartesian space is affected by both the angle and the distance from the U axis. Any inherent angular inaccuracies in the rotational axis are magnified as deposition occurs farther from the axis. The rings remain visible in the transverse method because they are aligned with the printing travel direction in this case, despite the less accurate model. Overall, the statement can be explored, that with future optimization, surface finish and overmolded print quality can be improved to the point where it parallels segmented printing. Potential areas of improvement include the mechanical components of the system, improved slicing and filtering algorithms, and filament variation capabilities. Also worthy of note, the standard deviation for the longitudinal models is less than that of the standard models, indicating that while they may not be as accurate to the reference mesh, the alternative process is repeatable and consistent.

4.3. Current Benefits and Future Directions

Indeed a benefit of the technology presented in a paper would be for training of physicians and/or helping them become more familiar with patient-specific anatomy. The above case study could currently be employed as a surgical planning tool, thereby providing physical models which can be handled and examined by physicians and patients prior to actual surgery. In the future, other features could be added to the seven-axis technology to fully realize the proposed patient-specific design scenario. For example, other moving printheads, such as powder direct energy deposition (DED) heads or screw-extrusion based nozzles, could replace the direct extruder shown, to allow for the use of filaments commonly associated with medical products, such as metal filaments or non-filamentous biocompatible compounds. In addition, the resolution of the system could be improved to match the resolutions of other common additive manufacturing methods. While lacking some of these developments, the study demonstrates potential advantages for incorporating additional additive manufacturing technology in the patient-specific design space, and provides an idealized pipeline for translating anatomy data into a patient-specific medical device prototype.

5. Conclusions

Additive manufacturing as a set of technologies has expanded in recent years. Many additive manufacturing methods are being used to great effect in the medical devices field for creating structures that are tailored to specific patient anatomy. However, limitations of this technology still exist. Before now, additive manufacturing systems have provided users with limited control over the local deposition orientation of material onto a workpiece, minimizing user-control over material properties and workpiece geometry. The seven degree-of-freedom additive manufacturing system described here solves a number of these problems, by allowing for the simultaneous control over the orientation of the deposition nozzle and the workpiece in 3D space. With this control, users can specify the local deposition properties of material via user-generated custom toolpaths as well as print on highly nonuniform surfaces in changing coordinate planes. These developments show promise beneficial to the patient-specific device prototyping field due to the suitability in working with highly nonuniform anatomical geometries. With continued improvement to the software and hardware components, seven-axis additive manufacturing systems will likely solve new challenges in patient-specific medical device design.

Supplementary Materials: The following supporting information can be downloaded at: <https://www.mdpi.com/article/10.3390/machines10121144/s1>. Video S1. Demonstration of the seven-axis system modifying the deposition nozzle angle around a single point. Video S2. Demonstration of the print bed tilting along the seven-axis system's V axis to create a structure with an overhang. Video S3. Demonstration of the print bed tilting along the seven-axis system's V axis to create a structure with angularly offset deposition layers. Video S4. Timelapse of the fabrication of a curved structure with angularly offset deposition layers.

Author Contributions: Conceptualization, J.M.H. and A.G.E.; methodology, J.M.H.; software, J.M.H.; validation, J.M.H. and A.G.E.; formal analysis, J.M.H.; investigation, J.M.H.; resources, J.M.H.; data curation, J.M.H.; writing—original draft preparation, M.L.; writing—review and editing, M.L. and A.G.E.; visualization, J.M.H.; supervision, A.G.E.; project administration, A.G.E.; funding acquisition, A.G.E. All authors have read and agreed to the published version of the manuscript.

Funding: This research was funded in part by Boston Scientific to match the 2017 University of Minnesota MN Robotics, Sensing, and Additive Manufacturing (RSAM) Drive grant. Further information is available in: <https://mndrive.umn.edu/robotics/funding/mndrive-rsam-industrial-partnership-grants>, accessed on 11 November 2022.

Data Availability Statement: The data presented in this study are available in: <https://conservancy.umn.edu/handle/11299/211762>, 11 November 2022.

Acknowledgments: The authors acknowledge the support of the Bakken Medical Devices Center, both financially and the prototyping facilities. The authors also acknowledge the financial support of Boston Scientific Corporation and University of Minnesota MN Drive grant program.

Conflicts of Interest: The authors declare no conflict of interest. The funders had no role in the design of the study; in the collection, analyses, or interpretation of data; in the writing of the manuscript; or in the decision to publish the results.

References

1. Hafez, M.A.; Moholkar, K. Patient-specific instruments: Advantages and pitfalls. *SCIOT-J* **2017**, *3*, 66. [[CrossRef](#)]
2. Gualdrón, C.I.L.; Ibarra, E.R.B.; Bohórquez, A.P.M.; Bohórquez, I.G. Present and future for technologies to develop patient-specific medical devices: A systematic review approach. *Med. Devices* **2019**, *12*, 253–273. [[CrossRef](#)] [[PubMed](#)]
3. Wong, K.C. 3D-printed patient-specific applications in orthopedics. *Orthop. Res. Rev.* **2016**, *8*, 57–66. [[CrossRef](#)] [[PubMed](#)]
4. Kolken, H.M.A.; Lietaert, K.; van der Sloten, T.; Pouran, B.; Meynen, A.; Van Loock, G.; Weinans, H.; Scheys, L.; Zadpoor, A.A. Mechanical performance of auxetic meta-biomaterials. *J. Mech. Behav. Biomed. Mater.* **2020**, *104*, 103658. [[CrossRef](#)]
5. Gueche, Y.A.; Sanchez-Ballester, N.M.; Cailleaux, S.; Bataille, B.; Soulairol, I. Selective Laser Sintering (SLS), a New Chapter in the Production of Solid Oral Forms (SOFs) by 3D Printing. *Pharmaceutics* **2021**, *13*, 1212. [[CrossRef](#)]
6. Tagliaferri, V.; Trovalusci, F.; Guarino, S.; Venettacci, S. Environmental and Economic Analysis of FDM, SLS and MJF Additive Manufacturing Technologies. *Materials* **2019**, *12*, 4161. [[CrossRef](#)] [[PubMed](#)]
7. Mazzoli, A. Selective laser sintering in biomedical engineering. *Med. Biol. Eng. Comput.* **2013**, *51*, 245–256. [[CrossRef](#)]
8. Ventola, C.L. Medical Applications for 3D Printing: Current and Projected Uses. *Pharm. Ther.* **2014**, *39*, 704–711.
9. Melčová, V.; Svoradová, K.; Menčík, P.; Kontárová, S.; Rampichová, M.; Hedvičáková, V.; Sovková, V.; Příkryl, R.; Vojtová, L. FDM 3D Printed Composites for Bone Tissue Engineering Based on Plasticized Poly(3-hydroxybutyrate)/poly(d,l-lactide) Blends. *Polymers* **2020**, *12*, 2806. [[CrossRef](#)]
10. Shaqour, B.; Samaro, A.; Verleije, B.; Beyers, K.; Vervaet, C.; Cos, P. Production of Drug Delivery Systems Using Fused Filament Fabrication: A Systematic Review. *Pharmaceutics* **2020**, *12*, 517. [[CrossRef](#)]
11. Chen, J.V.; Dang, A.B.C.; Dang, A. Comparing cost and print time estimates for six commercially-available 3D printers obtained through slicing software for clinically relevant anatomical models. *3D Print. Med.* **2021**, *7*, 1. [[CrossRef](#)] [[PubMed](#)]
12. Uno, M.; Sugimoto, K.; Taniguchi, I.; Tanaka, K. Six-Degree-of-Freedom Articulated Robot Mechanism and Assembling and Working Apparatus Using Same. U.S. Patent 5,197,846, 30 March 1990.
13. Zhang, H.; Liu, D.; Huang, T.; Qingxi, H.; Lammer, H. 3D Printing Method of Spatial Curved Surface by Continuous Natural Fiber Reinforced Composite. In Proceedings of the IOP Conference Series: Materials Science and Engineering, Qingdao, China, 28–29 December 2019; IOP Publishing: Bristol, UK, 2020; Volume 782, p. 022059.
14. Newell, C. Multiple Axis Robotic Additive Manufacturing System and Methods. U.S. Patent 11,198,252, 14 December 2021.
15. Hunter, L.W.; Brackett, D.; Brierley, N.; Yang, J.; Attallah, M.M. Assessment of trapped powder removal and inspection strategies for powder bed fusion techniques. *Int. J. Adv. Manuf. Technol.* **2020**, *106*, 4521–4532. [[CrossRef](#)]
16. Paul, R.; Anand, S.; Gerner, F. Effect of Thermal Deformation on Part Errors in Metal Powder Based Additive Manufacturing Processes. *J. Manuf. Sci. Eng.* **2014**, *136*, 031009. [[CrossRef](#)]

17. Zaeh, M.; Branner, G. Investigations on residual stresses and deformations in selective laser melting. *Prod. Eng.* **2009**, *4*, 35–45. [[CrossRef](#)]
18. Tang, M.; Pistorius, P. Anisotropic Mechanical Behavior of AlSi10Mg Parts Produced by Selective Laser Melting. *JOM* **2017**, *69*, 516–522. [[CrossRef](#)]
19. Laa, D. Fine Tune Your Resin 3D Print Supports. *Make* **2020**, *75*.
20. Martín-Montal, J.; Pernas-Sánchez, J.; Varas, D. Experimental Characterization Framework for SLA Additive Manufacturing Materials. *Polymers* **2021**, *13*, 1147. [[CrossRef](#)]
21. Tumbleston, J.R.; Shirvanyants, D.; Ermoshkin, N.; Janusziewicz, R.; Johnson, A.R.; Kelly, D.; Chen, K.; Pinschmidt, R.; Rolland, J.P.; Ermoshkin, A.; et al. Continuous liquid interface production of 3D objects. *Science* **2015**, *347*, 1349–1352. [[CrossRef](#)]
22. Dizon, J.R.; Gache, C.C.; Cascolan, H.M.S.; Cancino, L.T.; Advíncula, R. Post-Processing of 3D-Printed Polymers. *Technologies* **2021**, *9*, 61. [[CrossRef](#)]
23. Lee, C.S.; Kim, S.G.; Kim, H.J.; Ahn, S.H. Measurement of anisotropic compressive strength of rapid prototyping parts. *J. Mater. Process. Technol.* **2007**, *187–188*, 627–630. [[CrossRef](#)]
24. Sood, A.K.; Ohdar, R.K.; Mahapatra, S.S. Experimental investigation and empirical modelling of FDM process for compressive strength improvement. *J. Adv. Res.* **2012**, *3*, 81–90. [[CrossRef](#)]
25. Huss, J.M. Degree of Freedom Curvilinear Toolpath Generation for FDM 3D Printing with Applications in Patient-Specific Medical Device Prototyping. Ph.D. Thesis, University of Minnesota, Minneapolis, MN, USA, 2019.
26. Huss, J.M.; Erdman, A.G. Gravity Augmented Fused Filament Fabrication Additive Manufacturing. *J. Med. Devices* **2022**, *in press*.
27. FDA.gov. Available online: www.fda.gov/medical-devices/overview-device-regulation/regulatory-controls (accessed on 16 November 2022).
28. Zhao, G.; Ma, G.; Feng, J.; Xiao, W. Nonplanar slicing and path generation methods for robotic additive manufacturing. *Int. J. Adv. Manuf. Technol.* **2018**, *96*, 3149–3159. [[CrossRef](#)]
29. Folch, E.; Keyes, C. Airway stents. *Ann. Cardiothorac. Surg.* **2018**, *7*, 273–283. [[CrossRef](#)] [[PubMed](#)]
30. Sharma, N.; Aggarwal, L.M. Automated medical image segmentation techniques. *J. Med. Phys.* **2010**, *35*, 3–14. [[CrossRef](#)]
31. *Mimics*; Materialize NV: Leuven, Belgium, 2018.
32. *Cura*; Ultimaker: Utrecht, The Netherlands, 2018.
33. *Creality CR-10*; Creality: Shenzhen, China, 2019.
34. *MATLAB R2018b*; Mathworks: Natick, MA, USA, 2018.
35. Moller, T.; Trumbore, B. Fast, Minimum Storage Ray-Triangle Intersection. *J. Graph. Tools* **1997**, *2*, 21–28. [[CrossRef](#)]
36. Gneiting, T.; Ševčíková, H.; Percival, D.B. Estimators of Fractal Dimension: Assessing the Roughness of Time Series and Spatial Data. *Stat. Sci.* **2012**, *27*, 247–277. [[CrossRef](#)]
37. Meshlab; MeshLab 2016, General Public License, September 2016. Available online: <https://www.meshlab.net/> (accessed on 28 November 2022).
38. Cabrera, M.S.; Sanders, B.; Goor, O.J.G.M.; Driessen-Mol, A.; Oomens, C.W.J.; Baaijens, F.P.T. Computationally Designed 3D Printed Self-Expandable Polymer Stents with Biodegradation Capacity for Minimally Invasive Heart Valve Implantation: A Proof-of-Concept Study. *3D Print. Addit. Manuf.* **2017**, *4*, 19–29. [[CrossRef](#)]
39. Paunović, N.; Bao, Y.; Coulter, F.B.; Masania, K.; Geks, A.K.; Klein, K.; Rafsanjani, A.; Cadalbert, J.; Kronen, P.W.; Kleger, N.; et al. Digital light 3D printing of customized bioresorbable airway stents with elastomeric properties. *Sci. Adv.* **2021**, *7*, eabe9499. [[CrossRef](#)]